

# Matrix-free methods for the stability and control of boundary layers

Shervin Bagheri\*, Espen Åkervik†, Luca Brandt‡ and Dan S. Henningson§

*Linné Flow Centre, Department of Mechanics,  
Royal Institute of Technology, SE-100 44, Stockholm, Sweden*

This paper presents matrix-free methods for the stability analysis and control design of high-dimensional systems arising from the discretized linearized Navier-Stokes equations. The methods are applied to the two-dimensional spatially developing Blasius boundary-layer. A critical step in the process of systematically investigating stability properties and designing feedback controllers is solving very large eigenvalue problems by storing only velocity fields at different times instead of large matrices. For stability analysis, where the entire dynamics of perturbations in space and time is of interest, iterative and adjoint-based optimization techniques are employed to compute the global eigenmodes and the optimal initial conditions. The latter are the initial conditions yielding the largest possible energy growth over a finite time interval. The leading global eigenmodes take the shape of Tollmien-Schlichting wavepackets located far downstream in streamwise direction, whereas the leading optimal disturbances are tilted structures located far upstream in the boundary layer. For control design on the other hand, the input-output behavior of the system is of interest and the snapshot-method is employed to compute balanced modes that correctly capture this behavior. The inputs are external disturbances and wall actuation and the outputs are sensors that extract wall shear stress. A low-dimensional model that capture the input-output behavior is constructed by projection onto balanced modes. The reduced-order model is then used

---

\*Ph.D. Candidate, Mechanics, Student Member.

†Ph.D. Candidate, Mechanics, Student Member.

‡Assistant Professor, Mechanics.

§Professor, Mechanics, Member AIAA. The paper is based on the invited Julian D. Cole lecture given by the last author at the AIAA Theoretical Fluid Mechanics Conference, Seattle June 23-26, 2008

**to design a feedback control strategy such that the growth of disturbances are damped as they propagate downstream.**

## I. Introduction

Control of wall-bounded transitional and turbulent flows has been the subject of several research efforts owing to the high potential benefits. In these fluid-mechanics systems, due to the large flow sensitivity, dramatic effects on global flow parameters may be achieved by minute local perturbations using devices sensing and acting on only small parts of the flow with a small amount of energy. Such control devices can be used to obtain reduction of the skin-friction drag, for example, implying relevant savings of the operational cost of commercial aircrafts and cargo ships.

In this paper we perform stability analysis, model reduction and control design for the Blasius flow. The work is motivated by the need to provide efficient numerical tools to analyze complex flows and design efficient control strategies. Although we present results for the Blasius flow the methodology is applicable to any complex flow described by the direct and adjoint linearized Navier–Stokes equations. The techniques in this paper share a common methodology: very large eigenvalue problems are solved based only on snapshots of the velocity fields at different points in time. No large matrices are stored. Therefore the main tool is a code that time integrates the forward and adjoint linearized Navier–Stokes equations. This so called timestepper technique has become increasingly popular in both stability analysis<sup>1,2</sup> and for control design.<sup>3</sup>

It is now well understood that the wall-bounded flows are very sensitive to specific perturbations.<sup>4</sup> In particular, boundary layer flows support convective instabilities and behave as noise amplifiers.<sup>5</sup> Convectively unstable shear flows are stable from a global point of view;<sup>5,6</sup> wave packets generated locally, grow in amplitude as they travel downstream and finally decay or leave the observation window. This behavior can be captured by a non-modal analysis, see e.g. Ref. 7. It is therefore meaningful to analyze the spatial structure of the initial conditions and forcing yielding largest possible energy growth over a finite time interval. This optimization problem can be solved efficiently for more complex flows by solving the direct and adjoint Navier–Stokes equation for the linear evolution of perturbation about a steady state, as shown here (see also Ref. 2 or Ref. 8). The approach followed here requires only the use of a timestepper, a numerical code solving the Navier–Stokes equations, and avoids the use of the large matrices.

Two aspects in flow control have been identified as crucial in order to apply feedback control in more complex flows and to move towards an implementation in wind-tunnel tests. They are i) model reduction to significantly decrease the cost of both constructing the con-

troller and running it online, thus allow the fast computation of the control signal directly from the sensor output; ii) the need to naturally consider localized sensors and actuators.

Both these aspects are addressed in Bagheri *et al.*<sup>3</sup> In this paper, the results of Ref. 3 are extended by introducing wall actuation and wall shear stress measurements instead of idealized volume forcing actuation and velocity measurements inside the flow. The incorporation of actuators and sensors at the physical boundaries in our design, takes use one step closer to using the controller in actual experiments.

Model reduction becomes essential in order to apply modern control theoretical tools to fluid flow systems. For modern linear control, the aim is to build a model of low dimension that captures the input-output behavior of the Navier-Stokes system and use this model for optimal feedback control design. With the help of the adjoint Navier–Stokes equations two fundamental dynamical structures can be identified; the flow structures most easily influenced by the actuators considered and the flow structures to which the outputs are most sensitive. These so-called controllable and observable structures determine the input-output behavior completely for linear systems. It is well-known that these two set of modes can be balanced,<sup>10</sup> and represented by one set of non-orthogonal modes, called the balanced modes. These are used as a projection basis for model reduction. The approximated method employed to compute the balanced modes is the snapshot-based balanced truncation.<sup>11,12</sup> This method has been recently applied to the channel flow,<sup>13</sup> the flow around a pitching airfoil<sup>14</sup> and the Blasius flow.<sup>3</sup>

Recently, several groups have suggested and pursued the combination of computational fluid dynamics and control theory, thus going past early attempts of flow control based on physical intuition or on a trial-and-error basis (see the review in Ref. 15). The reader is also referred to Bagheri *et al.*<sup>9</sup> for a thorough review of the many tools used in flow control. In early work from our group,<sup>16,17</sup> a linear model-based feedback control approach, that minimizes an objective function which measures the perturbation energy, is formulated where the Orr-Sommerfeld and Squire equations model the flow dynamics. The latter equations describe the linear evolution of perturbations evolving in a parallel base flow. The control problem is combined with a state estimator: The so called Kalman and extended Kalman filter have been implemented in order to reconstruct the flow in an optimal manner by only considering continuous wall measurements. These studies have also shown the importance of physically relevant stochastic models for the estimation problem,<sup>18,19</sup> where stochastic noise needs to describe accurately enough the unmodeled dynamics, like uncertainties and nonlinearities. Based on these models the estimator is shown to work for both infinitesimal as well as finite amplitude perturbations in direct numerical simulations of transitional flows.<sup>20,21</sup> These studies however assumed a parallel base flow and distributed sensing and actuation at the wall.

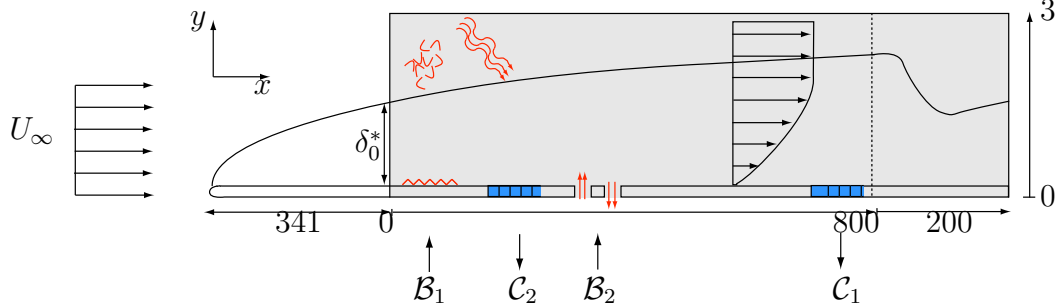


Figure 1. The input/output configuration used for the control of perturbations in a two-dimensional flat-plate geometry. The computational domain  $\Omega = (0, L_x) \times (0, L_y)$ , shown by the gray region, extends from  $x = 0$  to  $x = 1000$  with the fringe region starting at  $x = 800$ . The first input  $B_1$ , located at  $(x_w, y_w) = (35, 1)$ , models the initial receptivity phase, where disturbances are induced by free-stream turbulence, acoustic waves or wall roughness. The actuator,  $B_2$ , provides a mechanism to manipulate the flow, in this case by a wall blowing and suction centered at  $x_u = 400$ . Two sensors  $C_1$  and  $C_2$ , measuring the skin friction at the wall, are located at  $x_y = 300$  and  $x_z = 750$  respectively. The upstream measurements are used to estimate the incoming perturbations, while the downstream sensor quantifies the effect of the control.

The paper is organized as follows: The modal and nonmodal stability analysis is presented in section II. We start with describing the flow setup and formulating two eigenvalue problems. We continue with showing how the eigenvalue problems can be solved iteratively and finally present results for the Blasius flow. Section III deals with the control design. We introduce inputs, outputs and write the system in the state-space formulation. A brief summary of the LQG framework is provided before model reduction based on balanced modes is introduced. The snapshot method used for model reduction is explained and results on the performance of the reduced-order and controller are shown. Section IV provides concluding remarks.

## II. Stability Analysis

### II.A. Flow Configuration and the Initial Value Problem

We consider the two-dimensional incompressible flow over a flat plate with constant free-stream velocity  $U_\infty$  as shown in Figure 1. Starting from the leading edge a viscous boundary layer evolves downstream. The evolution of the streamwise velocity  $u$ , the wall-normal velocity  $v$  and the pressure  $p$  in time  $t$  and space  $(x, y)$  is governed by the incompressible non-linear Navier–Stokes equation.<sup>22</sup> Our analysis deals with the evolution of infinitesimal perturbations on this laminar boundary layer solution and is limited to the computational domain shown by the gray area in the figure: The inflow boundary is set to the downstream position corresponding to a Reynolds number  $Re_{\delta_0^*} = U_\infty \delta_0^* / \nu = 1000$ , where  $\delta_0^*$  is the local displacement thickness of the boundary layer and  $\nu$  is the kinematic viscosity. Throughout the paper all variables are non-dimensionalized by  $U_\infty$  and  $\delta_0^*$ . The length and height of the domain are  $L_x = 1000$  and  $L_y = 30$  in the streamwise direction  $x$  and wall-normal direction

$y$ , respectively.

The steady state, about which a linearization is performed, is obtained by marching the nonlinear governing equations in time. The linearized Navier-Stokes equations with boundary conditions can be cast (see *e.g.*<sup>3,23,24</sup>) as an initial-value problem in state-space form

$$\dot{\mathbf{u}} = \mathcal{A}\mathbf{u} \tag{1}$$

$$\mathbf{u} = \mathbf{u}_0 \quad \text{at} \quad t = 0. \tag{2}$$

with  $\mathbf{u} = (u, v)^T$ . However, in general, it is not always possible to have an explicit form for the operator  $\mathcal{A}$ , and, if possible, once it is discretized it will have very large dimension, i.e. the number of grid points times the number of velocity components  $n = 2N_xN_y$ . Our analysis will therefore be entirely based on the solution of the linearized Navier–Stokes equations that can be represented by an evolution operator

$$\mathbf{u}(\mathbf{x}, t) = \mathcal{T}(t)\mathbf{u}(\mathbf{x}, 0) = e^{At}\mathbf{u}_0. \tag{3}$$

The evaluation of the matrix exponential  $\mathcal{T}(t) = e^{At}$  is the key to both stability analysis, input-output analysis and control design, all of which will be discussed in the subsequent sections. However, this operator also poses the greatest computational challenge due its dimension. The dimension,  $n$ , of the linearized operator depends on the number of non-homogeneous spatial directions of the base flow. Except for one-dimensional base flows the exponential matrix must be approximated. The simplest methods require that all elements of the matrix can be stored in memory,<sup>25</sup> a requirement that cannot in general be met in fluid systems. As an example, the storage of the one dimensional Orr-Sommerfeld matrix for the evolution of disturbances in parallel flows requires approximately 1MB of memory, the system matrix for the present spatially inhomogeneous flow with the numerical scheme introduced above requires approximately 200GB, while the memory usage for a full three-dimensional system would be of the order of 200TB. However, the action of  $\mathcal{T}(t)$  on any flow field simply represents integrating the Navier-Stokes equations in time and therefore the exponential matrix can be approximated by numerical simulation of the governing equations, also referred to as a time-stepper. In what follows the reader should equate  $\mathcal{T}(t)\mathbf{u}(s)$  with a DNS simulation starting with an initial condition  $\mathbf{u}(\mathbf{x}, s)$  and providing  $\mathbf{u}(\mathbf{x}, t + s)$  at a later time. In this so called “timestepper approach”, system matrices are never stored and storage demands in memory are of the same order as a small number of flow fields. Numerically, the equations are solved with the pseudo-spectral Direct Numerical Simulation (DNS) code described in Ref. 26, where the spatial operators are approximated by Fourier expansion in the streamwise direction with  $N_x = 768$  equally distributed points and Chebyshev expansion

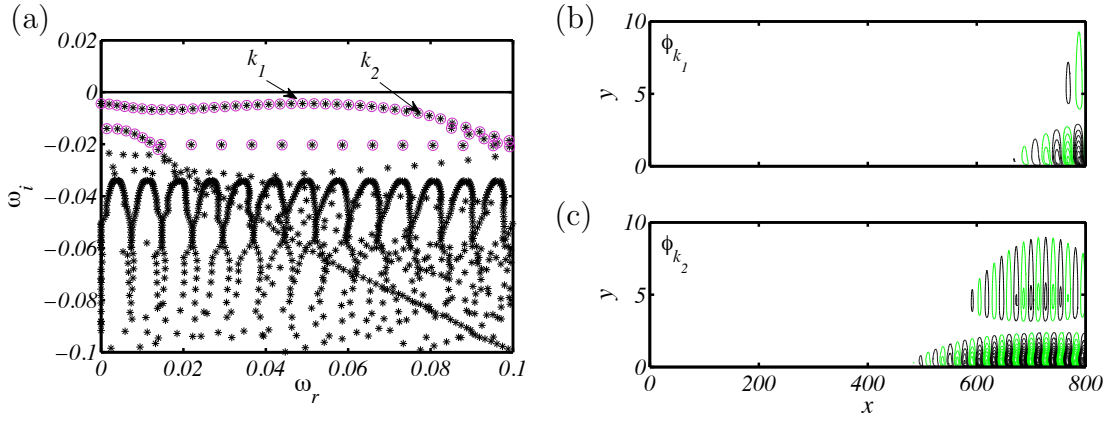


Figure 2. (a) Eigenvalues of  $\mathcal{A}$  as computed by the shift and invert Arnoldi method (shown as black stars) and eigenvalues computed by time-stepping using the evolution operator  $\mathcal{T}(t_f)$  (shown as magenta circles). The slightly damped eigenvalues, corresponding to Tollmien-Schlichting (TS) modes, and the freestream propagating modes are found by both methods. (b) Streamwise velocity component of the least stable TS eigenvectors, marked  $k_1$  in (a). (c) Streamwise velocity component of a high frequency but more damped TS mode, marked  $k_2$  in (a).

in the wall-normal direction on  $N_y = 101$  Gauss-Lobatto collocation points. A fringe region enforces periodicity in the streamwise direction.<sup>26</sup>

## II.B. Modal Stability

The first step in the understanding of the fluid problem at hand is examining the hydrodynamic stability of the flow, i.e. the behavior of infinitesimal disturbances to a base flow. In particular, modal stability deals with the response behavior of the baseflow to disturbances as time tends to infinity. This asymptotic response is governed by the eigenmodes of the evolution operator

$$\sigma_j \phi_j = \mathcal{T}(t_f) \phi_j, \quad |\sigma_1| > |\sigma_2| > \dots \quad (4)$$

for a fixed time  $t_f$  large enough. The stability of disturbances as  $t_f \rightarrow \infty$  is determined by the eigenvalue with the largest magnitude. If  $|\sigma_1| > 1$ , the system is linearly globally unstable. Note that the evolution operator  $\mathcal{T}$  has the same eigenfunctions as  $\mathcal{A}$  and the eigenvalues  $\lambda_j$  of  $\mathcal{A}$  can be related to those of  $\mathcal{T}$  through  $\lambda_j = \ln(\sigma_j)/t_f$ .

## II.C. Nonmodal stability

The amount of information obtained from (4) is limited to the asymptotic flow response and does not reveal the short time behavior of disturbances inherent to many flow systems. Relevant transient growth<sup>4</sup> of perturbations is indeed observed for many fluid dynamical systems due to the non-normality of the operator  $\mathcal{A}$  (an operator which does not commute with its adjoint) and nonmodal analysis is concerned with finding instabilities that are amplified in

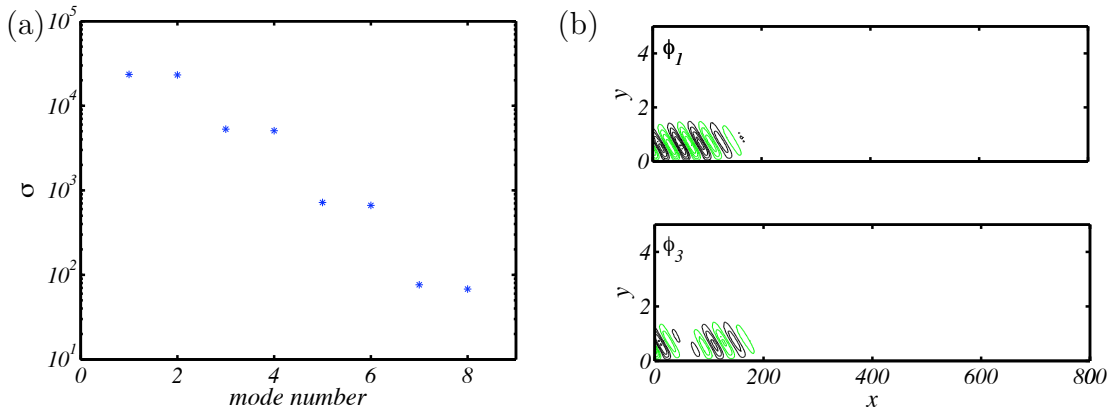


Figure 3. (a) Eigenvalues of  $\mathcal{T}^*\mathcal{T}$  computed using the forward and adjoint timestepper with  $t_m = 1800$ . (b) Streamwise velocity component of the optimal disturbance corresponding the largest eigenvalue in (a). (c) Streamwise velocity component of a suboptimal, corresponding to the third largest eigenvalue in (a).

a finite time interval. Furthermore, a competition between nonmodal and modal growth is observed in many systems, for example for three-dimensional perturbations in the Blaisus boundary layer.<sup>27</sup> For such flows, different transition scenarios can be observed depending on the external ambient noise. Therefore, in order to examine the largest possible disturbance growth due to all possible unit-norm initial conditions  $\mathbf{u}_0$  we will consider the energy associated to the disturbance at any time  $t_m$

$$\|\mathbf{u}(t_m)\|^2 = (\mathcal{T}(t_m)\mathbf{u}_0, \mathcal{T}(t_m)\mathbf{u}_0) = (\mathbf{u}_0, \mathcal{T}^*(t_m)\mathcal{T}(t_m)\mathbf{u}_0). \quad (5)$$

In the expression above the perturbation kinetic energy is the relevant norm ( $E = (\mathbf{u}, \mathbf{u})$ ) and the adjoint evolution operator  $\mathcal{T}^*(t_m)$  is introduced. Applying this operator corresponds to the integration of an adjoint state from time  $t_m$  to time 0. One can show<sup>3</sup> that an initial-value problem for the adjoint linearized Navier-Stokes equations governed by  $\mathcal{A}^*$  but with negative time derivative can be associated to the adjoint evolution operator  $\mathcal{T}^*$ . For a derivation of the adjoint operators in general we refer to Ref. 28 and for this particular setup to Ref. 3.

Initial conditions experiencing the largest nonmodal growth correspond to the leading eigenvalues of the operator  $\mathcal{T}^*(t_m)\mathcal{T}(t_m)$ , i.e.

$$\sigma_j \phi_j = \mathcal{T}^*(t_m)\mathcal{T}(t_m)\phi_j, \quad \sigma_1 > \sigma_2 > \dots > 0. \quad (6)$$

In particular, the first unit-norm eigenvector  $\phi_1$  is the optimal initial condition, resulting in the largest energy growth at time  $t_m$ . If its corresponding eigenvalue is larger than one,  $\sigma_1 > 1$ , the system can support nonmodal growth. The corresponding flow state at time  $t_m$  can be found by the evaluation of  $\mathcal{T}(t_m)\phi_1$ . In order to obtain a full map of the potential for transient growth the computations are repeated for different times  $t_m$ . Note that when

the system is discretized, we are again faced with a very large eigenvalue problem.

## II.D. Iterative Timestepping technique

The eigenvalue problems defined in (4) and (6) provide information about the modal and non-modal flow behavior of the system, respectively. The dimension of the matrices obtained by discretizing the operators appearing in (4) and (6) is too large to be solved by direct methods, such as the standard QR method. Therefore one has to resort to iterative methods, such as the Arnoldi,<sup>29</sup> which is based on the projection of the large matrix onto a lower-dimensional subspace. This results in a significantly smaller system that can be solved with direct methods. In addition, as mentioned above, in many cases only instantaneous velocity fields at different times are available. A particular subspace is the Krylov  $\mathcal{K}$  spanned by snapshots taken from flow fields separated by a constant time interval  $\Delta t$ ,

$$\mathcal{K} = \text{span}\{\mathbf{u}_0, \mathcal{F}(\Delta t)\mathbf{u}_0, \mathcal{F}(2\Delta t)\mathbf{u}_0, \dots, \mathcal{F}((m-1)\Delta t)\mathbf{u}_0\} \quad (7)$$

with  $\mathcal{F}(t) = \mathcal{T}(t)$  (modal stability) or  $\mathcal{F}(t) = \mathcal{T}^*(t)\mathcal{T}(t)$  (nonmodal stability) and  $\mathbf{u}_0$  is the initial guess that should contain nonzero components of the eigenmodes. By orthonormalizing  $\mathcal{K}$  with an  $m$ -step Arnoldi factorization we obtain a unitary basis  $\mathbf{V}$  on the which  $\mathcal{F}$  can be projected on;  $\mathcal{F}(\Delta t) \approx \mathbf{V}\mathbf{H}\mathbf{V}^T$ . This leads to a small eigenvalue problem of the form  $\mathbf{H}\mathbf{S} = \mathbf{\Sigma}\mathbf{S}$  which can easily be solved to recover the eigenmodes by  $\Phi = \mathbf{V}\mathbf{S}$ . In the case of global eigenmodes the eigenvalues of the system operator  $\mathcal{A}$  are given by  $\mathbf{\Lambda} = \ln(\mathbf{\Sigma})/\Delta t$ .

## II.E. Results

Results on modal and non-modal stability of the two-dimensional perturbations of the Blasius boundary layer are presented in this section. As mentioned above, the flow under investigation here is locally unstable but globally stable. Locally unstable perturbations, the Tollmien-Schlichting waves, grow while travelling downstream eventually leaving our control domain. From a global point of view the flow is then stable since disturbances have to be continuously fed upstream to avoid that the flow returns to its undisturbed state at each streamwise position. However, a significant transient growth of the disturbance energy in the domain is associated to the propagation of the unstable wave-packet.<sup>30,31</sup> This is also referred to as streamwise non-normality.<sup>6,32</sup>

### II.E.1. Modal stability

For two-dimensional perturbations of the Blasius boundary layer flow the memory requirements are still small enough to enable the storage of the system matrix  $A$ , the discretized

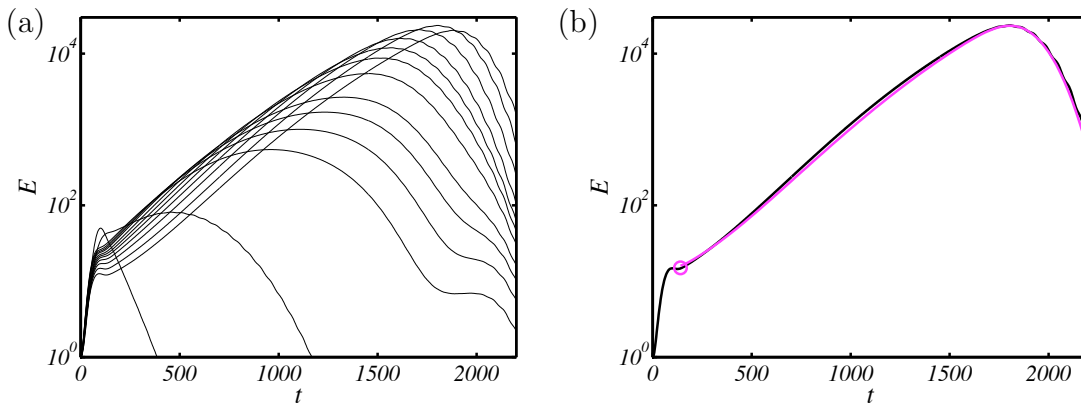


**Figure 4.** (a) Energy growth when optimizing for different times. The maximum is achieved for time  $t_m = 1800$  for which the maximum energy is  $E = 2.35 \cdot 10^4$ . (b) Thin black line repeats the energy evolution leading to the maximum growth at  $t_m = 1800$ , whereas thick magenta line shows the energy evolution obtained when projecting the system onto a small number of eigenvectors related to the TS branch in Figure 2(a). The latter clearly does not account for the initial gain due to the Orr mechanism, but by rescaling and shifting in time the two curves collapse, showing that the long time evolution is governed by propagating TS waves.

operator  $\mathcal{A}$ , in memory; the leading eigenmodes from the matrix eigenvalue problem  $\lambda_j \phi_j = \mathcal{A} \phi_j$  can thus be obtained by means of the shift and invert Arnoldi procedure. Figure 2(a) shows the eigenvalues obtained by the shift and invert matrix method as black stars. In the spectrum, one can identify several branches which all can be related to corresponding modes in the spectrum of a parallel Blasius boundary layer, as found by solving the Orr-Sommerfeld equations, though modified by non-parallelism and boundary conditions.<sup>31</sup> The upper branch can be identified as pure Tollmien-Schlichting (TS) waves. These modes are characterized by slightly damped eigenvalues with the corresponding eigenvectors obtaining their maximum values inside the boundary layer while decaying exponentially in the free stream. More stable modes can be associated to modes of the continuous spectrum, that is modes oscillating in the free stream and decaying inside the boundary layer.

Figure 2(b) and figure 2(c) show two examples of TS eigenvectors associated with eigenvalues marked  $k_1$  and  $k_2$  in Figure 2(a). As a consequence of the convective nature of the instabilities arising in the Blasius flow where disturbances grow in amplitude as they are convected in the downstream direction, the global eigenmodes are located far downstream where the flow energy is the largest. The streamwise wavelength of the eigenvectors increases as we go towards lower frequencies. The wall normal structure of these modes are very similar to those obtained by local temporal analysis in the framework of the Orr-Sommerfeld equation. The amplitude of the waves is exponentially increasing downstream: this, together with the temporal decay rate given by the eigenvalue, accounts for the spatial behavior of the mode. The matrix-free method based on the timestepper introduced in section II.D successfully locates the least damped eigenvalues by solving the eigenvalue problem (4). The eigenvalues are shown as magenta circles in figure 2(a), and are in perfect agreement with the results

obtained by the matrix method.

It is noteworthy that all the eigenvalues are damped, indicating that we will never observe the evolution of single eigenmodes in the flow, but rather we should focus our attention on the non-modal behavior, in other words the transient growth scenario. Note that it is possible to project the system (5) on a set of eigenmodes obtained from (4), thereby approximating the flow dynamics by a low-dimensional model living in the space spanned by a finite number of eigendirections.<sup>4</sup> For globally unstable flows, only one or few eigenmodes may be sufficient to capture the physical mechanism of the instability, see e.g. the shallow rounded cavity flow in Ref. 33, where an oscillating cycle could be captured by the sum of two unstable eigenmodes. However for a boundary layer flow like that studied here, it is shown in Ref. 31 that  $\mathcal{O}(1000)$  eigenmodes are needed to capture the full instability mechanism. With the present discretization and boundary conditions, moreover, the sum of the 1500 eigenmodes obtained from the Arnoldi method is not able to correctly describe the Orr mechanism<sup>4,31,34</sup> as obtained by the optimization via the time-stepper defined in (6). This is most likely due to the presence of eigenmodes related to the fringe region among the least damped eigenmodes. This points to the limitations of using eigenvalues as a general tool to study stability of complex systems characterized by strong non-normality.

### *II.E.2. Nonmodal stability*

Figure 3 shows the spectrum and two eigenfunctions of the eigenvalue problem (6) computed using the timestepper with  $t_m = 1800$ . Since  $\mathcal{T}^*\mathcal{T}$  is a self-adjoint positive-definite operator, its eigenvalues are real and positive. Moreover, the eigenvalues shown in figure 3a come in pairs. The corresponding velocity fields have the same wavepacket structure 90 degrees out of phase, representing traveling structures. The most unstable mode, i.e. the optimal disturbance and a suboptimal mode are shown in figure 3(b). They both have a spatial support far upstream, where the sensitivity of the flow is the largest. The modes are tilted in the upstream direction, “leaning” against the shear layer. As noticed by Ref. 35, the upstream tilting of the optimal initial conditions can be attributed to the wall-normal non-normality of the governing operator; perturbations extract energy from the mean shear by transporting momentum down the the mean velocity gradient (the so-called Orr mechanism). It is also noteworthy to remark on the separation of the spatial support of the optimal disturbance modes shown in figure 3(b)(far upstream) and global eigenmodes shown in figure 4(far downstream). This separation is associated to streamwise non-normality of the system.<sup>6</sup> Finally, note that there is nearly one order of magnitude between the energy of first pair and second pair of modes shown in figure 3(a). As a consequence, one can expect the inherent selection of disturbances in a randomly forced flow that resembles the flow response obtained when using the optimal disturbance as initial condition.

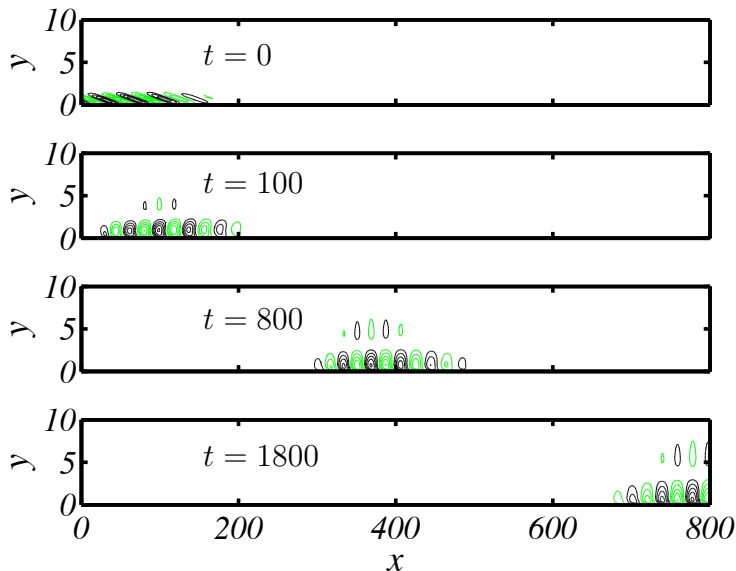


Figure 5. Time evolution for streamwise velocity with the combined Orr and TS mechanism, when initiated with the optimal initial condition from  $t_m = 1800$ . Note that the maximum amplitude is growing from frame to frame following the energy evolution given in Figure 4(b).

The energy evolution when solving for the largest eigenvalues of (6) at times  $t = \{100, 200, \dots, 2000\}$  is reported in figure 4(a). When optimizing for short times the optimal initial condition consists of upstream tilted structures that exploit the Orr mechanism only<sup>31</sup> to extract energy from the flow. Increasing the optimization time, the upstream-tilted structures move upstream, towards the start of our computational domain, weighting the possibility of growth due to the local Orr mechanism with the energy gain associated to the amplification and propagation of TS waves. The maximum energy growth in this box is obtained for final time  $t_m = 1800$ . The corresponding optimal initial condition is shown in the top frame in Figure 5. In figure 4(b) we compare the energy evolution due to this optimal initial condition with the energy evolution obtained when projecting (6) onto the space spanned by a small number of modes, all part of the TS branch in Figure 2. The evolution in the reduced system clearly does not capture the initial energy gain due to the Orr mechanism; however by rescaling the energy curve and shifting it in time to account for the initial gain due to the Orr mechanism, the subsequent evolution (amplification and propagation of the TS waves) is almost perfectly matching that of the full system. This results indicates that when computing optimal perturbations in the space spanned by some of the system eigenvalues care has to be taken in checking the general validity of the results.

The detailed evolution of the streamwise velocity due to the optimal initial condition at time  $t = 1800$  is shown in Figure 5. At the initial time the structures are leaning backwards against the shear. During the initial phase of the development the disturbance is raised

up, gaining energy through the Orr mechanism<sup>4,34</sup> and forming a wavepacket consisting of TS-waves. The wavepacket then propagates downstream, grows in size and finally leaves the computational domain; the energy evolution for this flow is reported in figure 4(b).

Modes	EVP	Snapshots	Method
Global modes	$\mathcal{T}\phi = \sigma\phi$	$\mathcal{T}(j\Delta t)\mathbf{u}_0$	Arnoldi
Optimal disturbances	$\mathcal{T}^*\mathcal{T}\phi = \sigma\phi$	$\mathcal{T}^*(j\Delta t)\mathcal{T}(j\Delta t)\mathbf{u}_0$	Arnoldi
Balanced modes	$PQ\phi = \sigma\phi$	$\mathcal{C}\mathcal{T}^*(j\Delta t)\mathcal{T}(j\Delta t)\mathcal{B}$	Snapshot

Table 1. ss

### III. Control Design

#### III.A. Introducing Inputs and Outputs

The next step after the analysis of the internal dynamics of our linear system is to manipulate it or to control it. In particular, our objective is to minimize the perturbation energy resulting from the growth of instabilities during the transition process in order to suppress or delay turbulence. To this end, we introduce actuators and sensors, or the inputs  $\mathcal{B}_1 w, \mathbf{u}_w \varphi$  and outputs  $\mathcal{C}_1, \mathcal{C}_2$  into our system;

$$\begin{aligned}
 \dot{\mathbf{u}} &= \mathcal{A}\mathbf{u} + \mathcal{B}_1 w, \\
 \mathbf{u}(x, 0, t) &= \mathbf{u}_w \varphi(t) = (0, v_w(x))^T \varphi(t), \\
 z(t) &= \mathcal{C}_1 \mathbf{u} \\
 y(t) &= \mathcal{C}_2 \mathbf{u}.
 \end{aligned} \tag{8}$$

where the wall actuation is a blowing and suction with function  $v_w(x)\varphi$  on the wall normal velocity with streamwise shape given by (36). The linearized Navier-Stokes equations represented by  $\mathcal{A}$  is now forced with external disturbances represented by the term  $\mathcal{B}_1(\mathbf{x})w(t)$  on the right-hand side of equation (8a). External disturbances enter the boundary layer upstream through some receptivity mechanism such as freestream turbulence or acoustic waves interacting with roughness as shown schematically in figure 1. In practice, the entire spatio-temporal evolution of disturbances is not available and it is therefore necessary to monitor the disturbance behavior through measurements. To accomplish this task, two sensors,  $\mathcal{C}_1$  and  $\mathcal{C}_2$  are introduced that measure the shear stress at the wall. The partial information of the incoming perturbations provided from the first sensor measurements ( $\mathcal{C}_1$  in figure 1) is used to reconstruct the actual flow dynamics by using a Kalman filter. Based on this flow estimation we can alter the behavior of disturbances by injecting fluid through blowing/suction holes in the wall. This type of actuation corresponds to imposing an inhomogeneous bound-

ary condition  $\mathbf{u}_w$  at the wall  $y = 0$  as given in equation (8b). Measurements provided by the second sensor  $\mathcal{C}_2$  located far downstream is used to determine whether our controller have been successful in reducing the shear stress at the wall. It thus plays the role of an objective function.

### III.B. The lifting procedure and state space formulation

Unfortunately, the formulation (8) based on wall actuation does not fit into the standard state-space formulation used in systems and control theory. Therefore, the boundary term  $\mathbf{u}_w(x)\varphi(t) = (0, v_w(x))^T\varphi$  is lifted into a volume forcing.<sup>36</sup> In the same manner as Ref. 37, we the solution  $\mathbf{u}$  is split into a homogeneous part  $\mathbf{u}_h$  and a particular part  $\mathbf{u}_p$ , so that  $\mathbf{u} = \mathbf{u}_h + \mathbf{u}_p$ . The particular solution fulfils the boundary conditions

$$\begin{aligned}\dot{\mathbf{u}}_p &= \mathcal{A}\mathbf{u}_p \\ \mathbf{u}_p(x, 0, t) &= (0, v_w(x))^T\varphi(t),\end{aligned}\tag{9}$$

and the homogeneous part satisfies homogeneous boundary conditions. In principle we can seek any solution  $\mathbf{u}_p$  of the above system, but one suitable choice is to use the steady steady state  $\mathcal{A}\mathbf{u}_p = 0$ . This is obtained by marching the DNS in time subject to steady ( $\varphi = 1$ ) wall blowing  $v_w(x)$  until a stationary state  $\dot{\mathbf{u}}_p = 0$  is obtained. In the following we denote this solution  $\mathcal{Z}(\mathbf{x})$ . The inhomogeneous boundary condition is satisfied by this solution, enabling us to write the particular solution for all times as  $\mathbf{u}_p = \mathcal{Z}\varphi$ , implying that the total field is given by  $\mathbf{u} = \mathbf{u}_h + \mathcal{Z}\varphi(t)$ . Again expressing the equation for  $\mathbf{u}$  in terms of the homogeneous and particular solution we get

$$\dot{\mathbf{u}}_h = \mathcal{A}\mathbf{u}_h + \mathcal{A}\mathcal{Z}\varphi - \mathcal{Z}\dot{\varphi} = \mathcal{A}\mathbf{u}_h + \mathcal{B}_2\dot{\varphi}.\tag{10}$$

Here we have used that  $\mathcal{A}\mathcal{Z} = 0$ . Further we have defined the input operator  $\mathcal{B}_2 = -\mathcal{Z}$  for the homogeneous system. The evolution of state and  $\varphi$  can be written as an augmented system for  $\hat{\mathbf{u}} = (\mathbf{u}_h, \varphi)^T$  as

$$\dot{\hat{\mathbf{u}}} = \hat{\mathcal{A}}\hat{\mathbf{u}} + \hat{\mathcal{B}}_2\phi, \quad \text{with} \quad \hat{\mathcal{A}} = \begin{pmatrix} \mathcal{A} & 0 \\ 0 & 0 \end{pmatrix}, \quad \hat{\mathcal{B}}_2 = \begin{pmatrix} \mathcal{B}_2 \\ 1 \end{pmatrix}, \quad \phi = \dot{\varphi}.\tag{11}$$

Note that in the lifted system (11) the control signal is given by time derivative of the boundary control signal,  $\phi = \dot{\varphi}$ . Similarly the input operator  $\mathcal{B}_1$  is extended to  $\hat{\mathcal{B}}_1 = (\mathcal{B}_1, 0)^T$  and the outputs are augmented to  $\hat{\mathcal{C}}_1 = (\mathcal{C}_1, \mathcal{C}_1\mathcal{Z})$  and  $\hat{\mathcal{C}}_2 = (\mathcal{C}_2, \mathcal{C}_2\mathcal{Z})$ .

The system (8) with inhomogeneous boundary condition can now be written in the stan-

standard state-space form

$$\dot{\mathbf{u}} = \mathcal{A}\mathbf{u} + \mathcal{B}\mathbf{f}, \quad (12)$$

$$\mathbf{y} = \mathcal{C}\mathbf{u} + \mathcal{D}\mathbf{f}, \quad (13)$$

where we have dropped the superscript  $\hat{\cdot}$ . Furthermore,  $\mathcal{B} = (\mathcal{B}_1, 0, \mathcal{B}_2)$  contains the two input operators,  $\mathcal{C} = (\mathcal{C}_1, \mathcal{C}_2)$  the two output operators,  $\mathbf{f} = (w, g, \phi)$  inputs time signals and  $\mathbf{y} = (y, z)$  the output time signals. We have introduced the additional feed-through term  $\mathcal{D}$  to model the effects of measurements noise ( $g$ ) and to penalize the actuation effort  $\phi$ ,

$$\mathcal{D} = \begin{pmatrix} 0 & 0 & l \\ 0 & \alpha & 0 \end{pmatrix}. \quad (14)$$

The outputs are now directly forced by in the inputs. The first output, or the objective function, can be written as  $z(t) = \mathcal{C}_1\mathbf{u} + l\phi$  which results in the objective functional<sup>a</sup>

$$\|z\|^2 = \int_0^\infty (\|\mathcal{C}_1\mathbf{u}\|^2 + l^2\phi^2) dt, \quad (15)$$

For large values of the scalar  $l$  the control effort is considered to be expensive, whereas small values indicate cheap control. The second output  $y(t) = \mathcal{C}_2\mathbf{u} + \alpha g$  is forced with noise  $g$  to model the uncertainty that may exist in the measurements under realistic conditions. It can be considered as a third forcing, but rather than forcing the Navier–Stokes equations it forces the measurements. Large values of the scalar  $\alpha$  indicate high level of noise corruption in the output signal, whereas for low values of  $\alpha$  the measurement  $y$  reflects information about the flow field with high fidelity.

### III.C. The LQG/ $\mathcal{H}_2$ Problem

The LQG/ $\mathcal{H}_2$  framework provides a controller that minimizes the cost functional (15). It is appropriate if the system operator  $\mathcal{A}$  accurately describes the flow dynamics, whereas a precise knowledge of external disturbances and the degree of noise contamination of the measurements are not available. We refer to Refs. 9, 39, 40 for further details on the  $\mathcal{H}_2$  control algorithm, as we will only outline the main steps here. The method can be extended (the so called  $\mathcal{H}_\infty$  method) in order to guarantee certain robustness properties. The control problem from an input-output viewpoint, or the  $\mathcal{H}_2$  problem, can be formulated as follows:

*Find an optimal control signal  $\phi(t)$  based on the measurements  $y(t)$  such that the in the*

---

<sup>a</sup>We assume that the cross weighting between the state and control signal is zero<sup>38</sup>

presence of external disturbances  $w(t)$  and measurement noise  $g(t)$  the output  $z(t)$  is minimized.

The determination of the control signal  $\phi$  is based only on the measurements from the sensor  $\mathcal{C}_2$ . However, for linear systems — due to the separation principle<sup>40</sup> — the feedback control law can be determined assuming that the complete velocity field is known. The forcing needed to reproduce the flow only from wall measurements can be computed independently. Hence, the design of the  $\mathcal{H}_2$ -controller is performed by solving two quadratic matrix equations called Riccati equations<sup>38</sup> that are independent of each other. They have the form

$$(\mathcal{A}\mathcal{Y} + \mathcal{Y}\mathcal{A}^* - \mathcal{Y}\mathcal{C}_2^*\mathcal{C}_2\mathcal{Y} + \mathcal{B}_2\mathcal{B}_2^*)\mathbf{u} = 0 \quad (16)$$

$$(\mathcal{A}^*\mathcal{X} + \mathcal{X}\mathcal{A} - \mathcal{X}\mathcal{B}_1^*\mathcal{B}_1\mathcal{X} + \mathcal{C}_2\mathcal{C}_2^*)\mathbf{u} = 0. \quad (17)$$

Solving the first Riccati equation we obtain the feedback type of control signal  $\phi = l^{-2}\mathcal{B}_2^*\mathcal{Y}\mathbf{u} = \mathcal{K}\mathbf{u}$ . The second Riccati equation provides the estimation feedback gain  $\mathcal{L} = -\alpha^{-2}\mathcal{X}\mathcal{C}_2^*$  so that the observer  $\dot{\hat{\mathbf{u}}} = (\mathcal{A} + \mathcal{L}\mathcal{C}_2)\hat{\mathbf{u}} + \mathcal{L}y$  can estimate the state  $\hat{\mathbf{u}}$  from the wall stress measurements. Finally, the compensator is obtained by the combination of these two as

$$\begin{aligned} \dot{\hat{\mathbf{u}}} &= (\mathcal{A} + \mathcal{B}_2\mathcal{K} + \mathcal{L}\mathcal{C}_2)\hat{\mathbf{u}} - \mathcal{L}y, \\ \phi &= \mathcal{K}\hat{\mathbf{u}}. \end{aligned} \quad (18)$$

This compensator runs online next to the experiments. Based on wall shear stress measurements  $y$  extracted by the first sensor, it provides an optimal control signal  $\phi$  proportional to the estimated flow  $\hat{\mathbf{u}}$ .

Any adequately accurate spatial discretization of the Navier-Stokes equations linearized about two or three dimensional baseflows results in a system with at least  $n \geq 10^5$  degrees of freedom. Due to the high dimensional state-space we can in general not solve the Riccati equations. Moreover, it would be very expensive to run the compensator online, since it has the same dimension as the full system. Therefore, to be able to apply modern control theoretical tools, it is important to construct a much smaller model of the Navier-Stokes system.

### III.D. The Model Reduction Problem and Balanced Truncation

The main features of the flow behavior which are relevant to preserve in the reduced order model is the input-output (I/O) behavior of the system, *i.e.* the relation between disturbances, wall actuation and the sensor outputs. Rather than investigating entire dynamics of

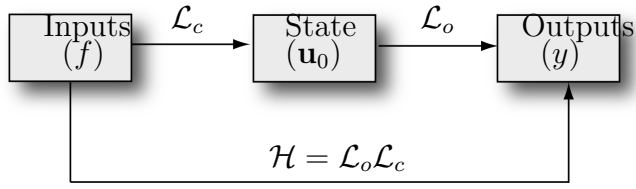


Figure 6. The operators used to examine the system input-output behavior. The controllability operator  $\mathcal{L}_c$  relates past inputs to the present state, while the observability mapping  $\mathcal{L}_o$  relates the present state to the future outputs. Their combined action is expressed by the Hankel operator  $\mathcal{H}$ .

flow fields at different times, the I/O behavior considers the time signals,  $\mathbf{f}(t)$  and  $\mathbf{y}(t)$ . Fortunately, the I/O behavior has significantly simpler dynamics compared to stability analysis where the entire flow dynamics is under investigation.

The model reduction problem for the preservation of input-output dynamics can be posed as following: Find the state-space system of order  $r \ll n$ ,

$$\begin{aligned}\dot{\kappa} &= A\kappa + B\mathbf{f}, \\ \hat{\mathbf{y}} &= C\kappa + D\mathbf{f}.\end{aligned}\tag{19}$$

so that for any input  $\mathbf{f}$  the difference between the output of the original and of the reduced system is small, i.e.

$$\sup_{\mathbf{f}} \frac{\|\mathbf{y} - \hat{\mathbf{y}}\|}{\|\mathbf{f}\|} = \|G - G_r\|_{\infty} \leq \epsilon_r\tag{20}$$

with  $\epsilon_r \ll 1$ . Equivalently, the model reduction error can be written in terms of the transfer functions associated  $G_r = C(sI - A)^{-1}B$  and  $G = C(sI - \mathcal{A})^{-1}\mathcal{B}$  in the frequency domain  $s \in \mathcal{C}$  instead of the time-domain.

One way to compute the reduced-order model (19) with a nearly minimal model reduction error (20) is called balanced truncation.<sup>10</sup> The method can be introduced in many different ways. In this section we will outline the method in manner that is reminiscent of the optimization problems that arise in the stability analysis. The presentation follows closely Bagheri *et al.*,<sup>3</sup> where also the definitions appropriate Hilbert spaces and adjoint operators are defined. Whereas, in stability analysis we were concerned with the properties of the evolution operator  $\mathcal{T}(t)$ , here our focus will lie on the so called Hankel operator<sup>41</sup> that maps input signals to output signals. In particular, it is defined as the mapping from past inputs  $\mathbf{f}(t) : t \in (-\infty, 0]$  to future outputs  $\mathbf{y}(t) : t \in [0, \infty)$ ,

$$\mathbf{y}(t) = \mathcal{H}\mathbf{f}(t) = C \int_{-\infty}^0 \mathcal{T}(t - \tau)\mathcal{B}\mathbf{f}(\tau) d\tau.\tag{21}$$

The amplification of the output signal at time  $t$  is given by

$$\|\mathbf{y}(t)\|^2 = (\mathcal{H}\mathbf{f}, \mathcal{H}\mathbf{f}) = (\mathbf{f}, \mathcal{H}^*\mathcal{H}\mathbf{f}). \quad (22)$$

In particular, the unit-norm input signals that result in the largest output response are the eigenmodes of  $\mathcal{H}^*\mathcal{H}$ , *i.e.*

$$\mathcal{H}^*\mathcal{H}\mathbf{f}_j = \sigma_j^2 \mathbf{f}_j, \quad \sigma_1 > \sigma_2 > \dots \quad (23)$$

where the square root of the eigenvalues  $\sigma_j^2$  are called the Hankel singular values (HSV). If  $\sigma_1 > 1$ , then the unit-norm input signal  $\mathbf{f}_1$  active in the past  $t \in (-\infty, 0]$  will generate an amplified output signal in the future  $t \in [0, \infty)$ .

Upper and lower bounds of the model reduction error for balanced reduced-order model of order  $r$  is given by the HSV as

$$\sigma_{r+1} < \|G - G_r\|_\infty \leq 2 \sum_{j=r+1}^n \sigma_j. \quad (24)$$

To obtain the balanced reduced-order model (19) and its associated transfer function  $G_r$  we project Navier-Stokes equations including inputs and outputs onto a set of bi-orthogonal modes, referred to as the balanced modes. These modes can be derived by decomposing the Hankel operator into  $\mathcal{H} = \mathcal{L}_o\mathcal{L}_c$  (shown schematically in Figure 6) which is possible since the operator (21) characterizes the I/O behavior via a reference state  $\mathbf{u}_0$ . In one part, the controllability operator  $\mathcal{L}_c$ , generates the reference state from past input signals, *i.e.*

$$\mathbf{u}_0 = \int_{-\infty}^0 \mathcal{T}(-\tau)\mathcal{B}\mathbf{f}(\tau) d\tau = \mathcal{L}_c\mathbf{f}(t). \quad (25)$$

The range of  $\mathcal{L}_c$ , *i.e.* the restriction of the state-space to all possible initial states that we are able to reach with  $\mathbf{f}(t)$  is called the controllable subspace. In particular the initial conditions that require the smallest input effort to reach are called controllable states and are the leading eigenmodes of the controllability Gramian

$$\mathcal{P} = \mathcal{L}_c\mathcal{L}_c^* = \int_0^\infty \mathcal{T}(\tau)\mathcal{B}\mathcal{B}^*\mathcal{T}^*(\tau) d\tau. \quad (26)$$

The other part of the Hankel operator is the observability operator  $\mathcal{L}_o$  operator which generates future outputs from the reference state,

$$\mathbf{y}(t) = \mathcal{C}\mathcal{T}(t)\mathbf{u}_0 = \mathcal{L}_o\mathbf{u}_0. \quad (27)$$

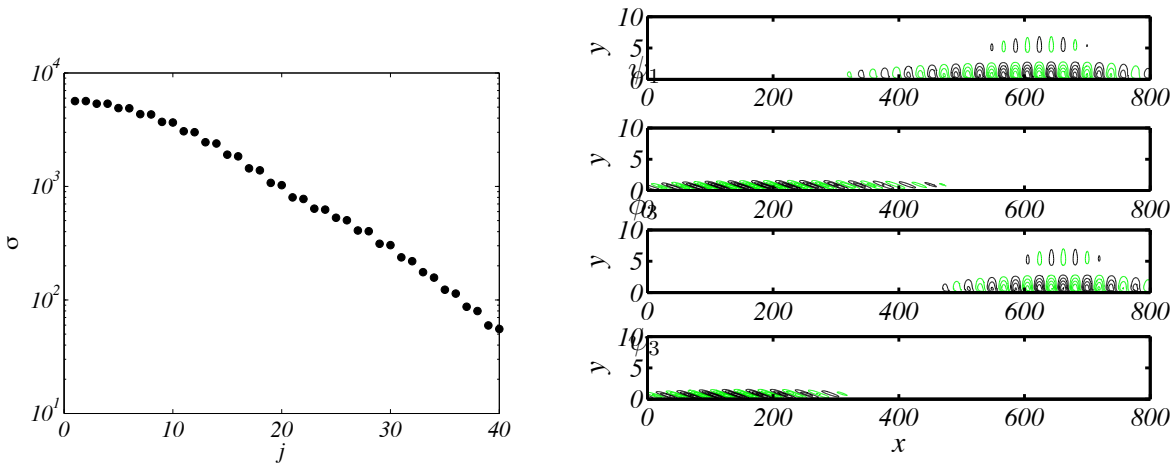


Figure 7. (1) Hankel Singular values. The streamwise velocity component of first and third direct (b,d)  $\phi_i$  and adjoint (c,e) balanced modes.

If  $\mathcal{L}_o \mathbf{u}_0 = 0$  for an initial condition  $\mathbf{u}_0$ , then  $\mathbf{u}_0$  is unobservable, since it cannot be detected by the sensors. The observable states on the other hand are initial conditions that are responsible for the largest output signals. These states are the leading eigenmodes of the observability Gramian,

$$\mathcal{Q} = \mathcal{L}_o^* \mathcal{L}_o = \int_0^\infty \mathcal{T}^*(\tau) \mathcal{C}^* \mathcal{C} \mathcal{T}(\tau) d\tau. \quad (28)$$

Using the mapping  $\mathcal{L}_c$  and  $\mathcal{L}_o$  we can now obtain the balanced modes  $\{\phi_j\}_{j=1}^m$  by mapping the most dangerous input signals  $\mathbf{f}_j$ , i.e. right eigenvectors of  $\mathcal{H}^* \mathcal{H}$  onto the state-space;  $\phi_j = \mathcal{L}_c \mathbf{f}_j$ . A set of modes that are bi-orthogonal to  $\phi_j$  ( $(\phi_i, \psi_j) = \delta_{i,j}$ ) can be found from  $\psi_j = \mathcal{L}_o^* \mathbf{g}_j$ , where  $\mathbf{g}_j$  are the left eigenvectors of the Hankel operator (see Ref. 3 for further details). The projection of the full Navier-Stokes equations on the balanced modes;  $A_{i,j} = (\psi_j, \mathcal{A} \phi_i)$ ,  $B_1 = (\psi_i, \mathcal{B}_1)$  and  $C_1 = \mathcal{C}_1 \phi_i$  results in the balanced reduced-order model (19).

Traditionally, the balanced modes are defined as the eigenvectors of the product of the controllability and observability Gramian. This formulation is easily obtained by noting that

$$\mathcal{L}_c \mathcal{H}^* \mathcal{H} \mathbf{f}_j = \mathcal{L}_c \mathcal{L}_c^* \mathcal{L}_o^* \mathcal{L}_o \mathcal{L}_c \mathbf{f}_j = \sigma_j^2 \mathcal{L}_c \mathbf{f}_j \quad (29)$$

resulting in the following eigenvalue problem for the balanced modes

$$\mathcal{P} \mathcal{Q} \phi_j = \sigma_j^2 \phi_j. \quad (30)$$

Similar to the modal and nonmodal analysis we end up with a very large eigenvalue problem when the state-space system is discretized.

### III.E. The Snapshot Method

In this section a brief summary of the snapshot method<sup>42</sup> for solving the eigenvalue problem (30) is presented. It is based on the recognition that the controllability and observability Gramians are the state correlation matrices generated from the impulse response of the forward and adjoint states respectively. The method for the computation of the balanced modes based on snapshots was introduced by Ref. 11 where it is also described in more detail.

The method has similarities to the Krylov-method presented earlier to compute global eigenmodes and optimal disturbances. This time, we will build two Krylov subspaces but avoid iterative techniques by exploiting the fact that the input and output spaces are much smaller than the state-space. In our case we have two inputs and two outputs (i.e.  $r = p = 2$ ) whereas the dimension of the state-space is approximately  $n = 10^5$ . The controllability and observability subspaces are, respectively,

$$\mathbf{X} = \text{span}\{\mathcal{B}, \mathcal{T}(\Delta t)\mathcal{B}, \mathcal{T}(2\Delta t)\mathcal{B}, \dots, \mathcal{T}((m-1)\Delta t)\mathcal{B}\} \quad (31)$$

$$\mathbf{Y} = \text{span}\{\mathcal{C}^*, \mathcal{T}^*(\Delta t)\mathcal{C}^*, \mathcal{T}^*(2\Delta t)\mathcal{C}^*, \dots, \mathcal{T}^*((m-1)\Delta t)\mathcal{C}^*\}. \quad (32)$$

Each element of  $\mathbf{X}$  contains snapshots from DNS simulations of the impulsive response of each input  $\mathcal{B}_i$ . Similarly, each element of  $\mathbf{Y}$  contains snapshots from adjoint DNS simulations of the impulse response of each output  $\mathcal{C}_i$ .

In a discretized setting,  $\mathbf{X}$  is a  $n \times (rm)$  matrix and  $\mathbf{Y}$  a  $n \times (pm)$  matrix. The Gramians can be approximated with  $\mathcal{P} \approx \mathbf{X}\mathbf{X}^T\Delta t$  and  $\mathcal{Q} \approx \mathbf{Y}\mathbf{Y}^T\Delta t$ . Thus the eigenvalue problem (29) can then be approximated as

$$\mathcal{P}\mathcal{Q}\phi_j \approx (\Delta t)^2 \mathbf{X}\mathbf{X}^H\mathbf{Y}\mathbf{Y}^H\phi_j = \sigma_j^2\phi_j. \quad (33)$$

This eigenvalue problem is of size  $n \times n$  and prohibitively expensive to solve for Navier-Stokes system. One can again resort to Arnoldi method and iterative techniques to solve the above eigenvalue problem as suggested in Ref. 12. However, this can be avoided by expanding the sought-after balanced modes in snapshots, i.e.  $\phi_j = \mathbf{X}\mathbf{H}_j$ . The column vector  $\mathbf{H}_j$  contains the expansion coefficients. This leads to small eigenvalue problem of size  $pm \times rm$  for  $\mathbf{H}$ ,

$$(\mathbf{X}\mathbf{Y}\mathbf{Y}^H\mathbf{X})\mathbf{H}_j = \sigma_j^2\mathbf{H}_j. \quad (34)$$

Usually the number of snapshots  $m$  times the number inputs ( $r$ ) or outputs ( $p$ ) is significantly smaller than the number of states  $n$ , which makes this method computationally tractable for systems of very large dimensions.

### III.F. Results

#### III.F.1. Performance of Reduced-Order Model

Figure 7 shows the spectrum and two eigenfunctions obtained by solving the eigenvalue problem (30) using the snapshot method. The first and third balanced modes and their associated adjoint modes compute are shown in figure 7(b). The singular values come in pairs  $(2n - 1, n)$ , resolving the  $n$ -th harmonics.<sup>3,13,14</sup> Therefore the second and fourth balanced mode looks like first and third mode respectively, but shifted in the streamwise direction. We observe that the leading balanced modes (figure 7a and c) appear as wavepackets located at the downstream end of the domain, whereas the adjoint balanced modes (figure 7b and d) are upstream tilted structures located at the upstream end of the domain. The adjoint modes are similar to the linear optimal disturbances shown in figure 5a and the balanced modes are similar to global eigenmodes shown in figure 2b. The adjoint balanced modes thus account for the output sensitivity and the direct balanced modes for the most energetic structures.

The projection of the full Navier-Stokes equations on the balanced modes;  $A_{i,j} = (\psi_j, \mathcal{A}\phi_i), B_1 = (\psi_i, \mathcal{B}_1)$  and  $C_1 = \mathcal{C}_1\phi_i$  results in the reducer-order model (19). The model reduction error (20) is shown in figure 8(a) together with the theoretical bounds given by the Hankel singular values in (24). The infinity norm of the transfer function equals the peak value of the frequency response. Estimating the model reduction error amounts to the calculation of the difference of the peak values of the reduced-order and the Navier–Stokes system. We observe the error norm remains approximately within the bounds given by the Hankel singular values for the first 50 modes. Higher modes become increasingly ill-conditioned and as a consequence the numerical round-off errors increase, the bi-orthogonality condition is gradually lost and the reduced system is no longer balanced. However, the singular values shown figure 7 decrease rapidly, indicating that the I/O behavior of the chosen setup can be captured by a low-dimensional model.

To investigate this, the amplitudes of the transfer functions with  $s = i\omega$ , *i.e.* the frequency response, are displayed in figure 8(b) for reduced-order models of order  $r = 2, 40$  and  $70$  and for the full DNS model of order  $10^5$ . All frequencies in the interval  $[0, 0.13]$  are amplified and the most dangerous frequency, *i.e.* the peak response of the full model is approximately  $\omega = 0.051$ . From figure 8(b) we observe that the reduced-order model of order 2 captures the most important aspect of the input-output behavior, which is the response of the most dangerous frequency. The model with 40 modes is able to estimate the gains of all the amplified frequencies, but fails to capture the damped low and high frequencies. Adding 30 additional modes results in a model that preserves the input-output behavior correctly for nearly all frequencies.

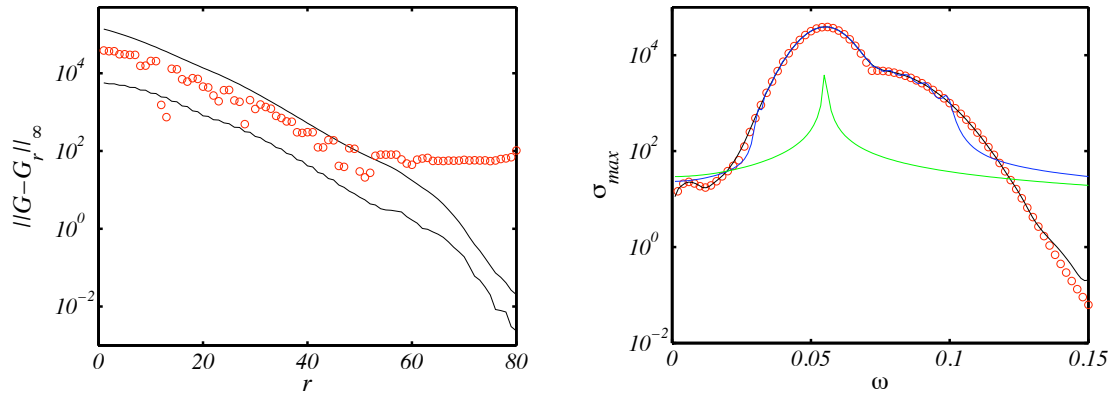


Figure 8. (a) The error at capturing the peak frequency is shown with red symbols. The upper and lower theoretical bounds are depicted with black lines. (b) The largest singular values  $\sigma$  of the transfer function  $|G(i\omega)|$  from all input to all outputs computed using the time-stepper is shown with red symbols. The largest response is for  $\omega = 0.06$  with a peak value of 144.6. The frequencies in the grey domain are amplified. The frequency response of the reduced model with rank 2 (green), 40 (blue) and 74 (black). Note that already the small model with rank 2 locates the frequency where the original system is most amplified.

Finally, the impulse responses from all inputs to all outputs of the reduced-order model (19) are compared to the full Navier–Stokes system (12). In figure (9) three signals  $\mathcal{B}_1 \rightarrow C_1$ ,  $\mathcal{B}_1 \rightarrow C_2$  and  $\mathcal{B}_2 \rightarrow C_1$  are shown with black lines. The response of  $C_2$  to forcing in  $\mathcal{B}_2$  is zero, since disturbances traveling upstream are quickly damped. These impulse responses were obtained by using the time-stepper with  $\sim 10^5$  degrees of freedom. The impulse responses of the reduced-order model (19) with  $r = 70$  given by  $y(t) = Ce^{At}B$  are shown with red dashed lines. We observe that reduced-model registers the same signal as the full model from all inputs to all outputs. The wavepacket triggered by the impulse of  $\mathcal{B}_1$  reaches the first sensor  $C_2$  after 600 time units and the second sensor  $C_1$  after 1500 time units. The wavepacket triggered from the actuator  $\mathcal{B}_2$  reaches the second sensor after 600 time units.

### III.F.2. Performance of Controller

In this section a reduced-order feedback controller, with the same dimension as the reduced-order model ( $r = 70$ ) of the previous section, is developed. The closed-loop behavior of the system and the objective function will be investigated and compared to the uncontrolled case for the flat-plate boundary layer flow. In particular, the output  $z$  of the closed-loop, i.e. the compensator (18) connected to the full Navier–Stokes model (8)) is compared to the linearized Navier–Stokes equations without control when the system is forced with stochastic excitation or initiated with an optimal disturbance.

Three controllers are investigated; (i) cheap control/low noise contamination with control penalty  $l = 1$  and noise parameter  $\alpha = 10^2$ , (ii) expensive control/high noise contamination with  $l = 10^2$  and  $\alpha = 10^7$  and (iii) an intermediate case with  $l = 10$  and  $\alpha = 10^5$ .

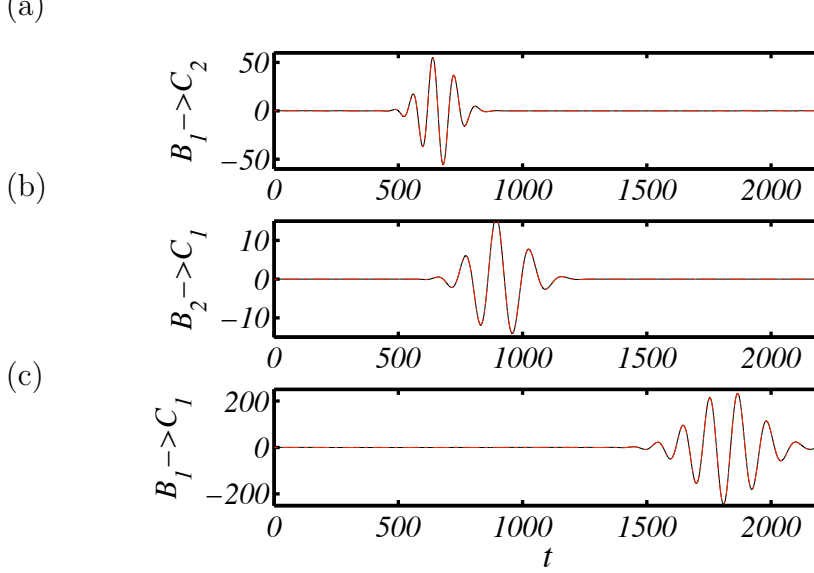


**Figure 9.** The impulse response from  $B_1 \rightarrow C_2$  (a),  $B_2 \rightarrow C_1$  (b) and  $B_1 \rightarrow C_1$  (c). The black solid line represents direct numerical simulations with  $10^5$  degrees of freedom and the red dashed line the balanced reduced-model with 50 degrees of freedom.

The performance of the cheap controller in case (i) for the control of the optimal initial condition discussed in Section II is examined first. This is interesting because the controller is not designed specifically for this configuration and it only has a limited window in time to counteract the disturbances that are propagating through the domain in the form of a localized wavepacket. In figure 10(a) the full domain kinetic energy as a function of time is shown as a solid black line for the uncontrolled evolution and as a dashed line for the controlled case. The effect of the controller is evident. The measurement signal detected by the sensor  $C_2$  is shown in figure 10(b) revealing that the sensor picks up the front of the wavepacket arriving at  $t \approx 350$ . A time lag of  $\approx 300$  consistent with the speed of the propagating wavepacket ( $0.3U_\infty$ ) is observed until the controller starts acting on the information (see figure 10(c)). The downstream measurement, *i.e.* the objective function to be minimized, is shown in figure 10(d) as a black solid line for the uncontrolled case and as a dashed black line for the controlled case. It can be seen that also this measure shows a satisfactory performance of the controller.

The three different controllers are tested on a flow case which is forced by the upstream disturbance input  $B_1$  with a random time signal. The wall-normal maximum of the rms-values of the streamwise velocity component in cases with and without control are shown in figure 11. The rms-value grows exponentially downstream in the uncontrolled case until the fringe region at  $x = 800$ . The rms of the controlled perturbation grows only until it reaches the actuator position where it immediately begins to decay. At the location of the objective function  $C_1$  ( $x = 750$ ), the amplitude of the perturbations is one order of magnitude smaller

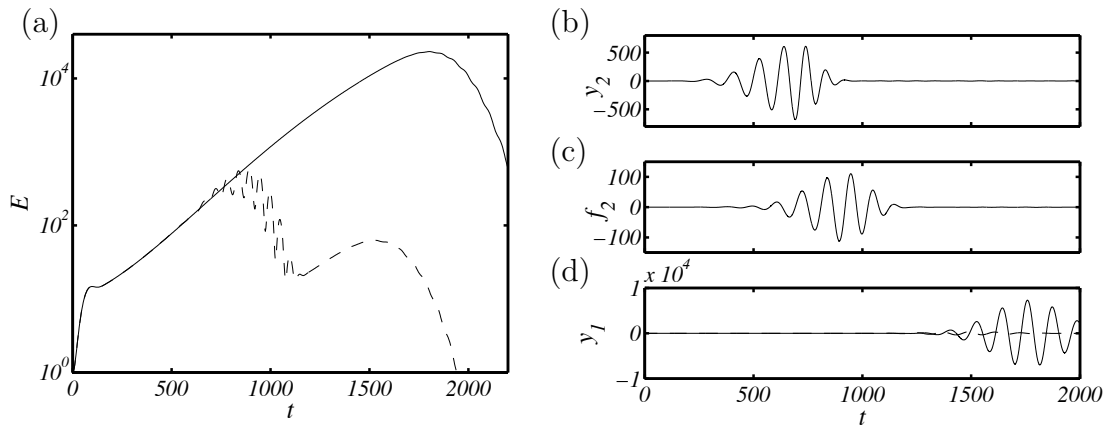


Figure 10. Control of the wavepacket due to the worst case initial condition. (a) Solid black line shows uncontrolled energy evolution (as in figure 4 (b)) and dashed black line shows the energy for the cheap controller. (b) Output signal as measured by the sensor  $C_2$  driving the controller. (c) Control signal fed into the wall actuator. (d) Signals from the sensor  $C_1$  measuring the objective function. Solid black line shows uncontrolled case whereas dashed black line shows the controlled case.

than in the uncontrolled case for the cheapest controller.

The rms values in the case of the expensive (case ii) and intermediate control (case iii) are shown with dashed and dashed-dotted lines respectively. The expensive control is very conservative as the measurement signals are highly corrupted and the control effort limited; it results only in a small damping of the disturbances. The intermediate controller (case iii) is more cautious in reducing the perturbation energy just downstream of the actuator when compared to the cheap controller. It is interesting to note, however, that at the location where the objective function is measured, the disturbance amplitude has decreased nearly as much as with the cheap controller, although the total perturbation energy is larger over the entire domain.

## IV. Conclusion

A framework for the stability and input-output analysis, model reduction and control design of complex flows is presented based on matrix-free methods. The two-dimensional Blasius boundary-layer flow is used here as example of a spatially inhomogeneous flow characterized by a strong non-normal operator governing the linear evolution of velocity perturbations.<sup>6</sup> The approach followed here requires only the numerical solution of the Navier–Stokes equations and of the associated adjoint problem. It avoids therefore the manipulation of large matrices and can be extended to fully three-dimensional flows and more complex geometries.

It is shown how the stability of complex flows can be investigated by considering the eigenvalues of the governing linear operator computed through iterative methods. However, the boundary layer flow considered here is characterized by convective instabilities and is

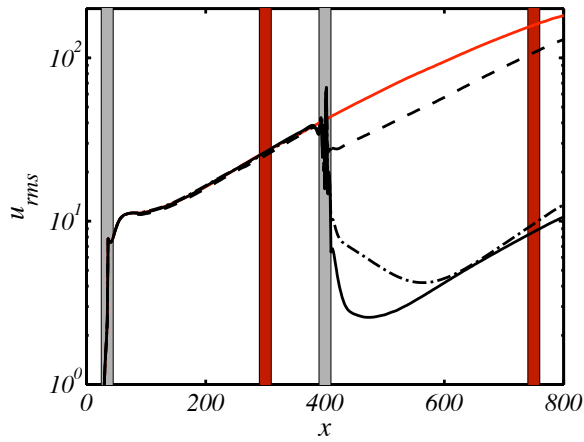


Figure 11. The rms-values of the uncontrolled system (red line), cheap controller (solid black), intermediate controller (dashed-dotted line) and expensive controller (dashed line). The gray bar represent the size (defined as 99% of the spatial support) and location of the two inputs, whereas the red bars correspond to the two outputs.

therefore stable in a global sense. The amplification of unstable waves traveling downstream and leaving the control domain can be seen in this context as transient growth. Non-modal analysis becomes therefore the correct tool to analyze these flows.<sup>6,7</sup> Optimal initial conditions yielding the largest possible energy growth over a finite time horizon are obtained for the Blasius boundary layer by integrating the Navier-Stokes direct and adjoint equations in time. The results reproduce and extend those previously obtained by expanding the flow into the eigenmodes of the system.<sup>31</sup>

To apply tools from modern control theory to fluid flow systems with many degrees of freedom model reduction becomes unavoidable. To build a low-order model of the problem the main features of the flow behavior are investigated in an input-output framework. The quantity one wishes to optimize for is now defined by a sensor output, in our case the level of perturbations further downstream, while information to the controller is provided by a sensor located upstream. Perturbations are introduced by the inputs considered in the model: the input furthest upstream models incoming disturbances while a second actuator is used to manipulate the flow. The balanced modes are computed from snapshots of the flow as introduced in Ref. 11.

Model reduction is achieved by projecting the governing equations on the leading balanced modes of the system. We show that the input-output behavior of the flat-plate boundary layer can be captured accurately with a reduced-order model based on seventy balanced modes. These modes are shown to provide a good description of the flow<sup>9,13</sup> since the account for both observability and controllability through a non-orthogonal projection. The spatial structure of these modes reflect the location of sensors/actuators and the dynamics of linear perturbation evolving in a boundary layer. The balanced modes are mainly located

downstream, where the response to the forcing is largest. The adjoint balanced modes are instead located upstream, where the sensitivity to initial conditions is the largest.

Finally, the low-order model is used to obtain the feedback gain relating directly the measurements from one upstream sensor to the actuator signal using the  $\mathcal{H}_2$  (LQG) formulation. The control is then applied in the numerical simulation of the full system where we show that the perturbations growth could be reduced efficiently. The present formulation accounts naturally for localized sensors and actuators and therefore, it can be directly applied to different flow configurations. Further, the control law derived from the low-order system can be applied on-line in an experiment provided accurate modeling of the sensor and actuator is available for the I/O analysis.

## A. Inputs and outputs

The expression of inputs  $\mathcal{B}_1, \mathbf{u}_w$  and outputs  $\mathcal{C}_1$  and  $\mathcal{C}_2$  are given in this section. The input  $\mathcal{B}_1$  is modelled by Gaussian type of volume forcing

$$\begin{bmatrix} \sigma_{w,x}\gamma_{w,y} \\ -\sigma_{w,y}\gamma_{w,x} \end{bmatrix} \exp(-\gamma_{w,x}^2 - \gamma_{w,y}^2), \quad \gamma_{w,x} = \frac{x - x_w}{\sigma_{w,x}}, \quad \gamma_{w,y} = \frac{y - y_w}{\sigma_{w,y}}, \quad (35)$$

with  $(\sigma_{w,x} = 4, \sigma_{w,y} = 0.25)$  determining the width and height of the function of the function centered around  $(x_w = 35, y_w = 1)$ . The actuator is in this case a localized zero mass-flux actuation on the wall-normal velocity,  $\mathbf{u}_w = (0, v_w)^T$  at the lower wall given by

$$v_w(x) = \left(1 - \left(\frac{x - x_u}{\sigma_{u,x}}\right)^2\right) \exp\left(-\frac{(x - x_u)^2}{2\sigma_{u,x}^2}\right), \quad (36)$$

with the width  $\sigma_{u,x} = 2.5$  and centered at  $x_u = 400$ . Finally, both measurements extract approximately the wall normal derivative of the streamwise velocity component (wall shear stress) in limited regions at the wall

$$\int_{\Omega} \begin{pmatrix} \gamma_{s,x}\gamma_{s,y}\mathcal{D}_y & 0 \end{pmatrix} \begin{pmatrix} u \\ v \end{pmatrix} d\Omega, \quad \gamma_{s,x} = \exp\left(-\frac{(x - x_s)^2}{\sigma_{s,x}^2}\right), \quad \gamma_{s,y} = \frac{1}{\sigma_{s,y}} \exp\left(-\frac{y^2}{\sigma_{s,y}^2}\right), \quad (37)$$

with  $x_e = 300$  for the output  $\mathcal{C}_2$  and  $x_e = 750$  for  $\mathcal{C}_1$ . The width of the regions are determined by  $\sigma_{s,x} = 5$  for both sensors. The operator  $\mathcal{D}_y$  denotes the  $y$ -derivative. The  $y$ -dependent weighting relies on a width parameter  $\sigma_{s,y} = 0.05$ . Note that in the limit  $\sigma_{s,y} \rightarrow 0$  the function approaches the delta function so that (37) defines the exact wall wall shear stress at the wall. The reason for using an approximation to the wall shear stress is the need for

an adjoint sensor  $\mathcal{C}^*$  (see Section III.D), which is derived with the respect to the signal to state inner product<sup>3</sup>

$$(r, \mathcal{C}\mathbf{u})_s = (\mathcal{C}^*r, \mathbf{u})_\Omega. \quad (38)$$

These inner products are defined as

$$(r, s)_s = s^T r \quad \text{and,} \quad (\mathbf{p}, \mathbf{q})_\Omega = \int_\Omega \mathbf{p}^T \mathbf{q} \, d\Omega. \quad (39)$$

for the scalars  $s$  and  $k$ , and the states  $\mathbf{q}$  and  $\mathbf{p}$ . The adjoint sensor obtained from this definition is in other words

$$(r, \mathcal{C}\mathbf{u})_s = \int_\Omega r^T \begin{pmatrix} \gamma_{s,x} \gamma_{s,y} \mathcal{D}_y & 0 \end{pmatrix} \mathbf{u} \, d\Omega = \int_\Omega r^T \begin{pmatrix} 2y \gamma_{s,x} \gamma_{s,y} / \sigma_{s,y}^2 & 0 \end{pmatrix} \mathbf{u} \, d\Omega = (\mathcal{C}^*r, \mathbf{u})_{\hat{\Omega}}, \quad (40)$$

where we have used integration by parts and the boundary conditions in  $y$ . This leads to the recognition of the adjoint sensor in the definition of the observability Gramian (28) as

$$\mathcal{C}^* = \begin{pmatrix} 2y \gamma_{s,x} \gamma_{s,y} / \sigma_{s,y}^2 \\ 0 \end{pmatrix}. \quad (41)$$

## Acknowledgements

The authors would like to thank Antonios Monokrousos for assisting in the implementations and acknowledge the financial support from the Swedish Research Council (VR).

## References

- <sup>1</sup>Blackburn, A. M., Barkley, D., and Sherwin, S., “TCconvective instability and transient growth in flow over a backward-facing step,” *J. Fluid Mech.*, Vol. 603, 2008, pp. 271–304.
- <sup>2</sup>Barkley, D., Gomes, M. G., and Henderson, R. D., “Three-dimensional instability in flow over a backward-facing step,” *J. Fluid Mech.*, Vol. 473, 2002, pp. 167–190.
- <sup>3</sup>Bagheri, S., Brandt, L., and Henningson, D. S., “Input-output analysis, model reduction and control design of the flat-plate boundary layer,” *J. Fluid Mech.*, 2008, In press.
- <sup>4</sup>Schmid, P. J. and Henningson, D. S., *Stability and transition in shear flows*, Springer, 2001.
- <sup>5</sup>Huerre, P. and Monkewitz, P. A., “Local and Global Instabilities in Spatially Developing Flows,” *Annu. Rev. Fluid Mech.*, Vol. 22, 1990, pp. 473–537.
- <sup>6</sup>Chomaz, J. M., “Global Instabilities in Spatially Developing Flows: Non-normality and Nonlinearity,” *Ann. Rev. Fluid Mech.*, Vol. 37, 2005, pp. 357–392.
- <sup>7</sup>Schmid, P. J., “Nonmodal Stability Theory,” *Ann. Rev. Fluid Mech.*, Vol. 39, 2007, pp. 129–62.
- <sup>8</sup>Barkley, D., Blackburn, H., and Sherwin, S. J., “Direct optimal growth analysis for timesteppers,” *Int. J. Numer. Meth. Fluids*, Vol. 57, 2008, pp. 1435–1458.

- <sup>9</sup>Bagheri, S., Hoepffner, J., Schmid, P., and Henningson, D., “Input-Output Analysis and Control Design Applied to a Linear Model of Spatially Developing Flows,” *Appl. Mech. Rev.*, 2008, In press.
- <sup>10</sup>Moore, B., “Principal component analysis in linear systems: Controllability, observability, and model reduction,” *Automatic Control, IEEE Transactions*, Vol. 26, No. 1, 1981, pp. 17–32.
- <sup>11</sup>Rowley, C. W., “Model Reduction for Fluids Using Balanced Proper Orthogonal Decomposition,” *Int. J. Bifurc. Chaos*, Vol. 15, No. 3, 2005, pp. 997–1013.
- <sup>12</sup>Willcox, K. and Peraire, J., “Balanced Model Reduction Via the Proper Orthogonal Decomposition,” *AIAA J.*, Vol. 40, No. 11, 2002, pp. 2323–2330.
- <sup>13</sup>Ilak, M. and Rowley, C. W., “Modeling of Transitional Channel Flow Using Balanced Proper Orthogonal Decomposition,” *Phys. Fluids*, Vol. 20, 2008, pp. 034103.
- <sup>14</sup>Ahuja, S., Rowley, C. W., Kevrekidis, I. G., and Wei, M., “Low-dimensional Models for Control of Leading-edge Vortices: Equilibria and Linearized Models,” *AIAA Paper 2007-709, 45th AIAA Aerospace Sciences Meeting and Exhibit*, 2007.
- <sup>15</sup>Kim, J. and Bewley, T. R., “A Linear Systems Approach to Flow Control,” *Annu. Rev. Fluid Mech.*, Vol. 39, 2007, pp. 383–417.
- <sup>16</sup>Högberg, M. and Henningson, D. S., “Linear optimal control applied to instabilities in spatially developing boundary layers,” *J. Fluid Mech.*, Vol. 470, 2002, pp. 151–179.
- <sup>17</sup>Högberg, M., Bewley, T. R., and Henningson, D. S., “Relaminarization of  $Re_\tau = 100$  turbulence using gain scheduling and linear state-feedback control.” *Phys. Fluids*, Vol. 15, 2003, pp. 3572–3575.
- <sup>18</sup>Hoepffner, J., Chevalier, M., Bewley, T. R., and Henningson, D. S., “State estimation in wall-bounded flow systems. Part 1. Perturbed laminar flows,” *J. Fluid Mech.*, Vol. 534, 2005, pp. 263–294.
- <sup>19</sup>Chevalier, M., Hoepffner, J., Bewley, T. R., and Henningson, D. S., “State estimation in wall-bounded flow systems. Part 2. Turbulent flows,” *J. Fluid Mech.*, Vol. 552, 2006, 167–187.
- <sup>20</sup>Chevalier, M., Hoepffner, J., Åkervik, E., and Henningson, D. S., “Linear feedback control and estimation applied to instabilities in spatially developing boundary layers.” *J. Fluid Mech.*, Vol. 588, 2007, pp. 163–187.
- <sup>21</sup>Monokrousos, A., Brandt, L., Schlatter, P., and Henningson, D. S., “DNS and LES of estimation and control of transition in boundary layers subject to free-stream turbulence,” *Int. J. Heat Fluid Flow*, Vol. 29, No. 3, 2008, pp. 841–855.
- <sup>22</sup>White, F. M., *Viscous Fluid Flow*, McGraw–Hill, Inc, second edition ed., 1991.
- <sup>23</sup>Kreiss, G., Lundbladh, A., and Henningson, D., “Bounds for threshold amplitudes in subcritical shear flows,” *J. Fluid Mech.*, Vol. 1994, 1993, pp. 175–198.
- <sup>24</sup>Bewley, T., Temam, R., and Ziane, M., “A general framework for robust control in fluid mechanics,” *Physica D: Nonlinear Phenomena*, Vol. 138, 2000, pp. 360–392.
- <sup>25</sup>Molder, C. and Van Loan, C., “Nineteen dubious ways to compute the exponential of a matrix, twenty-five years later,” *Siam Review*, Vol. 45, 2003, pp. 3–000.
- <sup>26</sup>Chevalier, M., Schlatter, P., Lundbladh, A., and D.S., H., “A pseudo spectral solver for incompressible boundary layer flows,” *Technical Report, Trita-Mek*, Vol. 7, 2007.
- <sup>27</sup>Levin, O. and Henningson, D. S., “Exponential vs algebraic growth and transition prediction in boundary layer flow,” *Flow, Turbulence and combustion*, Vol. 70, 2003, pp. 183–210.
- <sup>28</sup>Giles, M. B. and Pierce, N. A., “Analytic adjoint solutions for the quasi-one-dimensional Euler equations,” *J. Fluid Mech.*, Vol. 426, 2001, pp. 327–345.

- <sup>29</sup>Lehoucq, R. B., Sorensen, D., and Yang, C., *ARPACK Users' Guide: Solution of Large-Scale Eigenvalue Problems with Implicitly Restarted Arnoldi Methods*, SIAM, Philadelphia, 1998.
- <sup>30</sup>Ehrenstein, U. and Gallaire, F., "On two-dimensional temporal modes in spatially evolving open flows: the flat-plate boundary layer," *J. Fluid Mech.*, Vol. 536, 2005, pp. 209–218.
- <sup>31</sup>Åkervik, E., Ehrenstein, U., Gallaire, F., and Henningson, D. S., "Global two-dimensional stability measures of the flat plate boundary-layer flow," *Eur. J. Mech. B/Fluids*, Vol. 27, 2007, pp. 501–513.
- <sup>32</sup>Cossu, C. and Chomaz, J., "Global measures of local convective instability," *Phys. Rev. Lett.*, Vol. 77, 1997, pp. 4387–90.
- <sup>33</sup>Åkervik, E., Hoepffner, J., Ehrenstein, U., and Henningson, D. S., "Optimal Growth, Model Reduction and Control in a Separated Boundary-layer Flow Using Global Eigenmodes," *J. Fluid. Mech.*, Vol. 579, 2007, pp. 305–314.
- <sup>34</sup>Orr, W. M. F., "The stability or instability of the steady motions of a perfect liquid and of a viscous liquid. Part I: A perfect liquid. Part II: A viscous liquid." *Proc. R. Irish Acad. A*, Vol. 27, 1907, pp. 9–138.
- <sup>35</sup>Butler, K. and Farrell, B. F., "Three-dimensional optimal perturbations in viscous shear flow," *Phys. Fluids A*, Vol. 4, 1992, pp. 1637–1650.
- <sup>36</sup>Curtain, R. and Zwart, H., *An introduction to infinite-dimensional linear systems theory*, Springer Verlag, New York, 1995.
- <sup>37</sup>Högberg, M., Bewley, T. R., and Henningson, D. S., "Linear feedback control and estimation of transition in plane channel flow," *J. Fluid Mech.*, Vol. 481, 2003, pp. 149–175.
- <sup>38</sup>Zhou, K., Salomon, G., and Wu, E., "Balanced Realization and Model Reduction for Unstable Systems," *Int. J. Robust Nonlinear Control*, Vol. 9, 1999, pp. 183–198.
- <sup>39</sup>Anderson, B. and Moore, J., *Optimal control: Linear Quadratic Methods*, Prentice Hall, New York, 1990.
- <sup>40</sup>Zhou, K., Doyle, J., and Glover, K., *Robust and Optimal Control*, Prentice Hall, New Jersey, 2002.
- <sup>41</sup>Glover, K., "All optimal Hankel-norm approximations of linear multivariable systems and the  $L^\infty$ -error bounds," *Int. J. Control*, Vol. 39, 1999, pp. 1115–1193.
- <sup>42</sup>Sirovich, L., "Turbulence and the Dynamics of Coherent Structures I-III," *Quart. Appl. Math.*, Vol. 45, 1987, pp. 561–590.